



High specific surface area LaFeCo perovskites—Synthesis by nanocasting and catalytic behavior in the reduction of NO with CO

R.K.C. de Lima^a, M.S. Batista^b, M. Wallau^c, E.A. Sanches^d, Y.P. Mascarenhas^d, E.A. Urquieta-González^{a,*}

^a Laboratory of Applied Catalysis, Department of Chemical Engineering, Federal University of Sao Carlos, Rodovia Washington Luis Km 235, C. Postal 676, CEP 13565-905, Sao Carlos, SP, Brazil

^b Postgraduate Program in Materials Sciences, Federal University of the Vale of Sao Francisco, C. Postal 252, CEP 56304-440, Petrolina, PE, Brazil

^c Institute of Chemistry and Geosciences, Federal University of Pelotas, C. Postal 354, CEP 96020-080, Pelotas, RS, Brazil

^d Institute of Physics of Sao Carlos, University of Sao Paulo, C. Postal 369, CEP 13560-970, Sao Carlos, SP, Brazil

ARTICLE INFO

Article history:

Received 18 October 2008

Received in revised form 15 February 2009

Accepted 2 April 2009

Available online 10 April 2009

Keywords:

Nanocasting

Carbon

La–Co–Fe perovskites

NO reduction

CO oxidation

ABSTRACT

LaFe_{1-x}Co_xO₃ perovskites were conventionally or nanocasting synthesized. The nanocasting involved the preparation of a micro-mesoporous carbon mould using a Silica Aerosil 200 and a carbon source. Then, perovskites were carbon cast at 800 °C. The solids were characterized by XRD, N₂ sorption, FTIR, TGA/DTG, SEM and TEM. N₂ sorption evidenced that the nanocast perovskites did not show significant intraparticle porosity in spite of their enhanced (30–50 m²/g) specific surface area (SSA). Nevertheless, TEM images, XRD and Rietveld refinement data showed that the solids are constituted at least by 97 wt% of perovskite phase and by agglomerates smaller than 100 nm constituted by crystallites of about 6 nm. TGA/DTG results demonstrated carbon oxidation during the perovskite formation, thus eliminating the template effect and facilitating the occurrence of sintering, which limited the SSA increase. The nanocast perovskites were more active in the reduction of NO than the uncast ones, behavior that was attributed to the increase in their SSA that allows the exposure of a higher number of accessible active sites. However, the perovskite composition and the presence of impurities can reduce the effect of the improvement of the textural properties. The nanocast perovskites also showed high thermal and catalytic stability, corroborating their potential as catalysts for the studied reaction.

© 2009 Elsevier B.V. All rights reserved.

1. Introduction

Perovskite-type mixed metal oxides have demonstrated high potential as catalysts, specially in the depollution of exhaust gases [1–5]. These solids have a well-defined crystalline structure represented by the general formula ABO₃, where A designates a cation of rare-earth, alkaline earth, alkali or ions with a large ionic radius, like Pb²⁺ or Bi³⁺ and B a transition metal cation from the groups 3d, 4d or 5d [6–10]. The formation of complex mixed oxides from the partial substitutions on A- and/or B-sites are possible and can generate a large variety of compounds with different compositions [11–15].

Such wide flexibility of metal composition is of great importance for heterogeneous catalysis since the substitution of A- and/or B-sites by other cations is accompanied by hard modifications of the catalytic properties of the material [16–18]. In addition, advantages such as their easy synthesis, low cost and

high thermal stability determine and justify the special interest raised by these materials in the last decades [19–21].

Since the 1970s, perovskites are reported as promising substitutes for noble metal based catalysts (in particular of palladium, platinum and rhodium), whose use for the exhaust gas cleaning is predominant nowadays [22–25]. However, the low specific surface areas of perovskites (<10 m²/g) prepared by conventional synthesis routes, limit their efficiency in catalytic processes [26–28]. In the last decades, great efforts have been done to obtain perovskites with increased specific surface area. Nevertheless, because the synthesis of perovskites is carried out through reactions, which occur in the solid state at high temperatures, the preparation of such binary, ternary or multinary oxides with high specific surface area is often difficult. As known, in such conditions severe sintering occurs, producing large particles with low specific surface area [29], while lower calcination temperatures lead to other phases besides perovskite [27].

Several preparation methods, as micro-emulsion, sol–gel, spray-drying, freeze-drying, citrate complexation, flame-hydrolysis and coprecipitation were attempted in order to reduce the disadvantages of conventional perovskite synthesis [30–36]. Usually, these methods need great amounts of organic liquids,

* Corresponding author. Tel.: +55 16 33518201; fax: +55 16 33518286.

E-mail address: urquieta@ufscar.br (E.A. Urquieta-González).

expensive reagents and/or precursors, besides to a complex and multi-step preparation sequences. Recently, some works related with the synthesis of inorganic compounds with improved textural properties have shown that these inconveniences may be overcome using the nanocasting technique [37–40].

As described by Valdés-Solís and Fuertes [41] in a recent review article, in the preparation of inorganic compounds by nanocasting, the materials are formed inside nanospaces provided by the empty space (i.e., pore channels) of a porous solid (hard template). After the synthesis of the nanocast material, the template is selectively removed and the inorganic product is obtained. Ideally, the used hard template must have an interconnected pore channels, thus the pore structure of the resulting nanocast solid should be an inverse replica of that template [42].

In this work we prepared perovskites with high specific surface areas using the nanocasting technique. Nanosized solids with LaFeO_3 and $\text{LaFe}_{0.6}\text{Co}_{0.4}\text{O}_3$ nominal compositions were synthesized using a porous carbon as hard template, which was obtained using Silica Aerosil 200 as cast. In order to evaluate the catalytic activity of the obtained perovskites, the environmentally relevant reduction of NO to N_2 using CO as reduction agent (Eq. (1)) was used as test reaction.



Also the oxidation of CO to CO_2 was verified. The reaction of NO with CO is very convenient since both reactants are undesirable pollutants and very common components in exhaust gases of mobile and stationary sources [43–45]. Finally, the catalytic activity of the perovskites prepared by nanocasting was compared with similar samples obtained by the conventional citrate complexation method.

2. Experimental

2.1. Preparation of perovskites by a conventional method

Typical $\text{LaFe}_{1-x}\text{Co}_x\text{O}_3$ ($x = 0$ or 0.4) perovskites were prepared by the citrate method [46], using salts of $\text{La}(\text{NO}_3)_3 \cdot 6\text{H}_2\text{O}$ (Fluka, 99.0%), $\text{Co}(\text{NO}_3)_2 \cdot 6\text{H}_2\text{O}$ (Riedel-de Haën, 99.0%) and $\text{Fe}(\text{NO}_3)_3 \cdot 9\text{H}_2\text{O}$ (97.0%) as inorganic precursors. In this conventional preparation, stoichiometric amounts of the nitrate salts were mixed and dissolved in deionised water. Then, equimolar amounts of citric acid (Vetec, 95.0%) and ethylene glycol (Synth, 99.5%) were added and the solution stirred at room temperature for 5 min. The excess of water in the mixture was evaporated in an oven at 60°C for 20 h. The resulting powder was grounded and then calcined under air flow in two heating steps: 550°C for 3 h and 800°C for 5 h (heating rate of 4°C min^{-1}).

2.2. Preparation of the porous carbon

The porous carbon was prepared following a slightly modified method published by Yu et al. [47]. Pyrogenic Silica Aerosil 200 (Degussa), which consists of aggregated silica spheres with mean diameters of 12 nm [48], was used as hard template. Firstly, Aerosil 200 was mixed with a concentrated aqueous solution of sucrose (66 wt%), containing $0.1 \text{ g H}_2\text{SO}_4 \text{ g}^{-1}$ of sucrose, and then kneaded with a spatula in order to obtain a uniform mixture. After drying in air overnight at room temperature and subsequently treated at 100°C for 5 h (heating rate 1°C min^{-1}), the sucrose was carbonized under nitrogen atmosphere at 800°C for 5 h (heating rate 1°C min^{-1}). Finally, the silica was removed by dissolution with hydrofluoric acid (40 wt%). The resulting carbon, denominated as $\text{C}_{\text{AEROSIL}}$, was washed with distilled water and finally dried at 100°C . For comparison purposes an amount of sucrose solution (66 wt% containing $0.1 \text{ g H}_2\text{SO}_4 \text{ g}^{-1}$ of sucrose) was also dried and

carbonized under the same conditions but in the absence of any silica. The resulting uncast carbon was denominated C_{UNCAST} .

2.3. Preparation of perovskites by nanocasting

$\text{LaFe}_{1-x}\text{Co}_x\text{O}_3$ ($x = 0$ or 0.4) perovskites were prepared using a strategy based on the nanocasting technique. Firstly, an aqueous solution was prepared containing the perovskite precursors as was described in Section 2.1. Then, to that solution was added a pre-established amount of $\text{C}_{\text{AEROSIL}}$ and the suspension stirred for 1 h. The excess of water in the suspension was evaporated in an oven at 60°C for 20 h. In order to convert the infiltrated perovskite precursors into their corresponding oxide phases, the carbon/inorganic-precursor composite was thermally treated under static air at 550°C for 3 h and then at 800°C for 5 h (heating rate of 4°C min^{-1}). To guarantee the complete elimination of the carbon mould, the obtained nanocast perovskite was thermally treated under air flow at 550°C for 6 h (heating rate of $10^\circ\text{C min}^{-1}$).

2.4. X-ray diffraction (XRD)

The powder diffraction patterns of the prepared uncast and nanocast perovskites were obtained in a Rigaku Multiflex diffractometer operated at 40 kV and 40 mA and using a Ni-filtered $\text{Cu-K}\alpha$ radiation ($\lambda = 1.5418 \text{ \AA}$). The X-ray analyses were performed in the range of 2θ angles from 15 to 90° with a goniometer rate of $0.5^\circ(2\theta) \text{ min}^{-1}$. The formation of the perovskite phase was confirmed according to JCPDS data [49] while the crystallite sizes were calculated using the Scherrer's formula [50].

2.5. Rietveld refinement

The Rietveld refinement method [51] was used to accurately identify and quantify the crystalline phases in the nanocast $\text{LaFe}_{0.6}\text{Co}_{0.4}\text{O}_3$ perovskite. X-ray diffraction was performed using a Rigaku RotaFlex operating with $\text{Cu-K}\alpha$ radiation, 50 kV, 100 mA equipped with a graphite monochromator. The data collection was recorded in the range of $2\theta = 20$ – 110° with a step of 0.02° and 3 s/step. Rietveld refinement was developed using the space group $Pbnm$ for $\text{La}((\text{Co}_{0.4}\text{Fe}_{0.6})\text{O}_3)$, taking the ones obtained by Karpinsky et al. [52] as initial parameters and the space group $P3m1$ for La_2O_3 , taking the ones obtained by Hirosaki et al. [53] as initial parameters. The FULLPROF suit program [54] was used for the Rietveld structure refinement [55], using the least-squares method [56] to achieve the best agreement between the measured and the calculated profile. Parameters of the Lanthanum Cobalt Iron Oxide and Lanthanum Oxide were obtained from the Inorganic Crystallographic Structure Database [57]. Thompson-Cox-Hastings pseudo-Voigt function was used as the profile function [58]. The parameters constituting the instrumental resolution function $(U, V, W)_{\text{instr}}$ were obtained from a LaB_6 standard ($U = 0.007405$, $V = -0.021296$, $W = 0.022455$).

2.6. N_2 sorption measurements

The specific surface area S_p (m^2/g) was calculated by the BET method [59] from the N_2 adsorption/desorption isotherms obtained at 77 K. The measurements were carried out on a Quantachrome Corporation Nova-1200 instrument. Prior to the analysis, the samples ($\sim 150 \text{ mg}$) were treated at 200°C for 2 h under vacuum. The pore size distribution was obtained from the desorption branch of the isotherm using the Barret–Joyner–Halenda (BJH) method [60].

2.7. Fourier transformed infrared (FTIR) spectroscopy

The FTIR spectra of the dried Aerosil/sucrose mixture and the porous carbon $\text{C}_{\text{AEROSIL}}$ were recorded using the KBr pellet

technique in a PerkinElmer Spectrum 100 FTIR spectrometer from 500 to 4000 cm^{-1} with 32 scans, 4 cm^{-1} resolution and an interval of 1 cm^{-1} .

2.8. Thermal analysis (TGA/DTG)

The porous carbon C_{AEROSIL} and the uncast perovskites were further studied by thermogravimetry (TGA/DTG) on a Thermal Analyst 2100 TA Instruments thermobalance from 25 to 1000 $^{\circ}\text{C}$ (heating rate of 10 $^{\circ}\text{C min}^{-1}$) under air flow using about 10 mg of the respective solid. In the case of the nanocast perovskites the TGA was performed under a static air and after the experiment the analyzed sample was cooled and submitted to a new TGA under air flow.

2.9. SEM and TEM images

Scanning electron microscopy (SEM) images were recorded using a Philips XL 30 FEG instrument. Previous to the analysis, a thin coating of gold sputter was deposited onto the samples. Transmission electron microscopy (TEM) was performed on a Philips CM-120 microscope.

2.10. Catalytic tests

The studied perovskites were evaluated in the reduction of NO with CO that was carried out under atmospheric pressure in a laboratory scale unit using a fixed bed quartz tubular reactor containing 100 mg of the catalyst and 100 mg of ground quartz (80 mesh). A mixture of commercial gases of 5000 ppm of NO and 5000 ppm of CO diluted in He (V/V), was fed continuously at a total rate of 50 mL min^{-1} , corresponding to a GHSV of 15,000 h^{-1} . The reactor was installed in a tubular furnace, with the temperature regulated by an electronic controller through a thermocouple maintained in contact with the catalyst bed. The feed stream and the reactor effluents were analyzed by online gas chromatography using a Shimadzu (GC-17A) instrument equipped with a thermal conductivity detector (TCD) and a two packed columns, one being a Porapack N and the other a Molecular Sieve 13X. Each perovskite was submitted at least to a two catalytic test in all range of the used temperatures (150–700 $^{\circ}\text{C}$). In order to obtain additional information about the catalytic stability of the nanocast perovskites, they were submitted to a long term evaluation at conversion level of NO lower than 100%. Thus, after the second test, the reactor was cooled to 380 $^{\circ}\text{C}$ and the reaction maintained at this temperature during 1400 min on stream.

3. Results and discussion

3.1. Characterization of the nanocast carbon

Fig. 1 shows the SEM micrograph of the pyrogenic Silica Aerosil 200 used as cast to prepare the porous carbon. The image reveals the presence of spherical agglomerates with mean diameters in the range of 10 μm . It is reported that the total specific surface area (S_{BET}) for this pyrogenic silica is $200 \pm 25 \text{ m}^2/\text{g}$ and that the silica agglomerates are build-up from smaller primary particles with diameters of around 12 nm [48].

The nitrogen isotherms of the nanocast carbon (C_{AEROSIL}) obtained using the Silica Aerosil 200 as mould and the carbon obtained by sucrose carbonization in the absence of any silica mould (C_{UNCAST}) are shown in Fig. 2. The specific surface area (S_{BET}), the external specific surface area (S_{ext}), the micropore surface area (S_{micro}), the total specific pore volume (V_{total}), the specific mesopore volume (V_{meso}) and the specific micropore volume (V_{micro}) observed for these carbons are summarized in Table 1

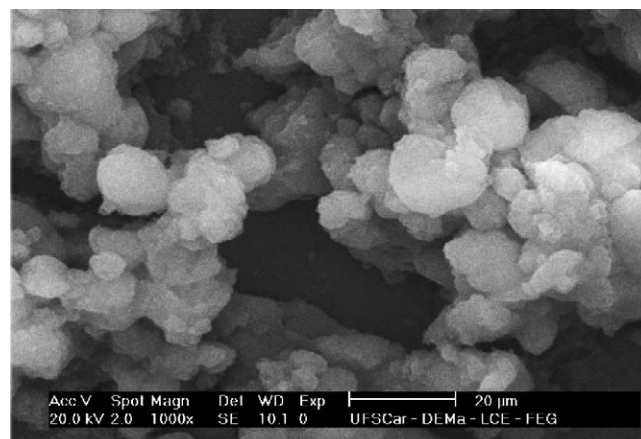


Fig. 1. SEM image of the pyrogenic Silica Aerosil 200.

together with the mean pore radius taken from the maximum of their BJH pore size distributions shown as an inset in Fig. 2.

As can be seen from the values given in Table 1, the nitrogen isotherms and the BJH pore size distribution of the C_{UNCAST} shown in Fig. 2, demonstrate that a low surface area carbon without any porosity is formed when the sucrose solution is dried and carbonized in the absence of a silica mould. On the other hand, when Silica Aerosil 200 was used as cast, the resulting N_2 isotherms of the nanocast carbon were a mixture of types I and IV. This indicates that a mesoporous carbon (C_{AEROSIL}) with a pore size distribution between 2 and 8 nm in diameters was obtained (inset in Fig. 2), which has a relatively large amount of micropores as it is revealed by its specific micropore volume (V_{micro}), reported in Table 1.

Fig. 3 shows the SEM micrograph of the C_{AEROSIL} that indicates the presence of agglomerates of carbon particles without a well-defined morphology, which should represent an inverse replica of the Silica Aerosil 200 agglomerates. The FTIR spectrum of the C_{AEROSIL} (not shown) confirmed the sucrose decomposition and did not show bands at around 1384 and 1596 cm^{-1} that would indicate the formation of graphite like structures [61–63].

The thermogravimetric analysis (TGA) and the differential thermogravimetric analysis (DTG) of the resulting porous carbon (C_{AEROSIL}) are shown in Fig. 4. As can be seen, the TG curve indicates two steps of weight loss at temperatures of around 68 and 638 $^{\circ}\text{C}$. These two steps are attributed, respectively, to desorption of water

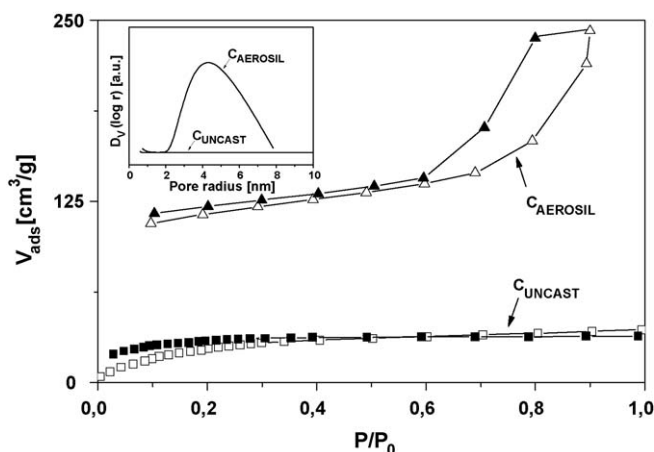
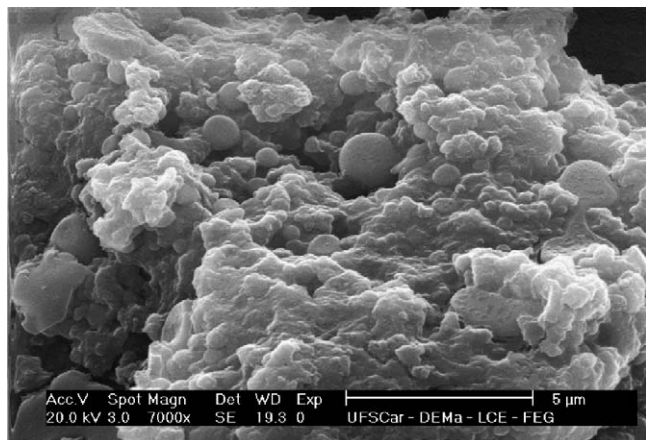


Fig. 2. Nitrogen adsorption/desorption isotherms of the nanocast carbon (C_{AEROSIL}) and the uncast carbon (C_{UNCAST}). The symbols indicate: (\blacktriangle , \blacksquare) adsorption; (\triangle , \square) desorption. Inset: BJH pore size distribution of the nanocast carbon (C_{AEROSIL}) and the uncast carbon (C_{UNCAST}).

Table 1

Textural properties of the prepared carbons.

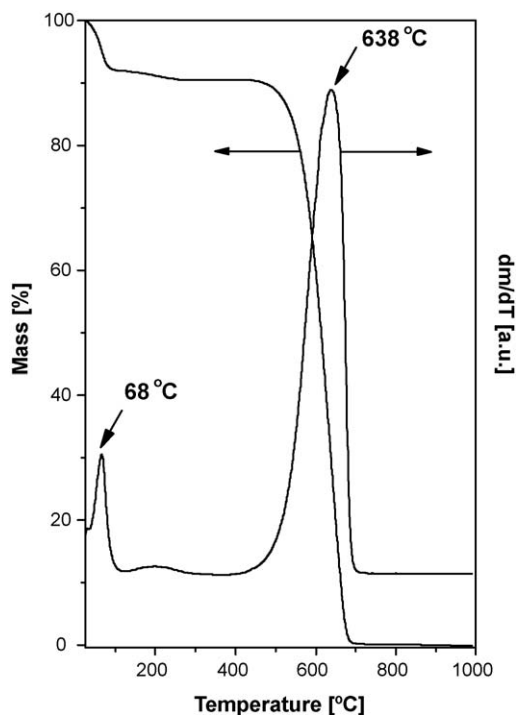
Sample	S_{BET} (m^2/g)	S_{ext} (m^2/g)	S_{micro} (m^2/g)	V_{total} (cm^3/g)	V_{meso} (cm^3/g)	V_{micro} (cm^3/g)	r_{pore} (nm)
C _{AEROSIL}	369	148	220	0.376	0.241	0.147	4.5
C _{UNCAST}	61	61	0	0.056	–	–	–

**Fig. 3.** SEM image of the nanocast carbon (C_{AEROSIL}).

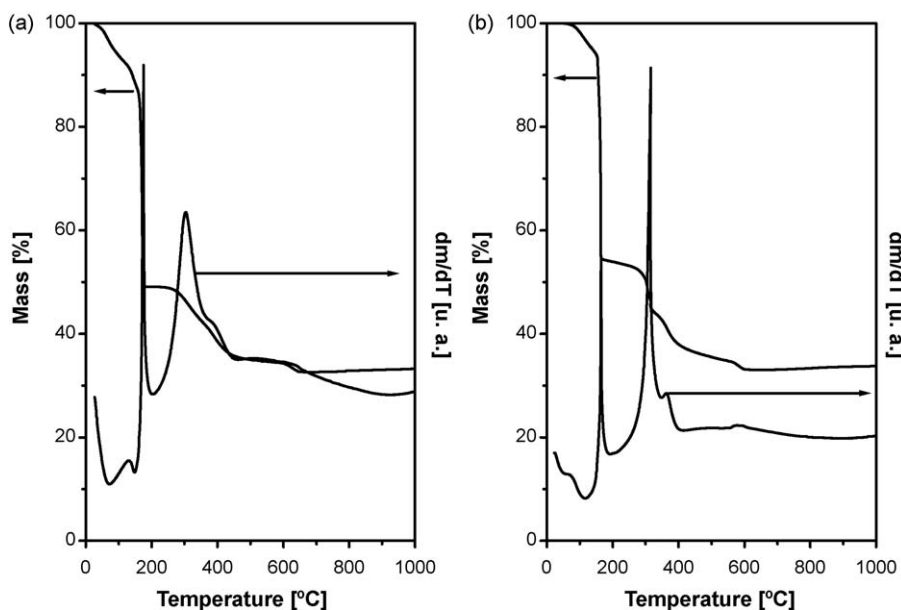
physically adsorbed and the carbon oxidation, which occurs without the formation of intermediates. From Fig. 4 it can further be observed that a mass loss of 100% occurred up to 690 °C. The fact that the carbon C_{AEROSIL} was completely burned off shows that the Silica Aerosil 200 used as mould was totally removed after the treatment with hydrofluoric acid.

3.2. Perovskites characterization

Fig. 5 shows the TG curves of the precursors of LaFeO₃ and LaFe_{0.6}Co_{0.4}O₃ perovskites conventionally prepared via the citrate method. It can be observed that the precursors transformation proceed through the typical mass loss steps [64] related with the elimination of adsorbed or hydrated water (up to ca. 150 °C);

**Fig. 4.** TGA/DTG curves of the nanocast carbon (C_{AEROSIL}).

evaporation and/or decomposition of some remaining citric acid (at ca. 200 °C); decomposition of ethylene glycol, nitrates and citrates into carbonates (225–400 °C); decomposition of carbonates species (400–600 °C) and formation of the final perovskite phase (above 600 °C).

**Fig. 5.** TGA/DTG curves of the inorganic perovskite precursor conventionally prepared by the citrate method: (a) LaFeO₃ and (b) LaFe_{0.6}Co_{0.4}O₃.

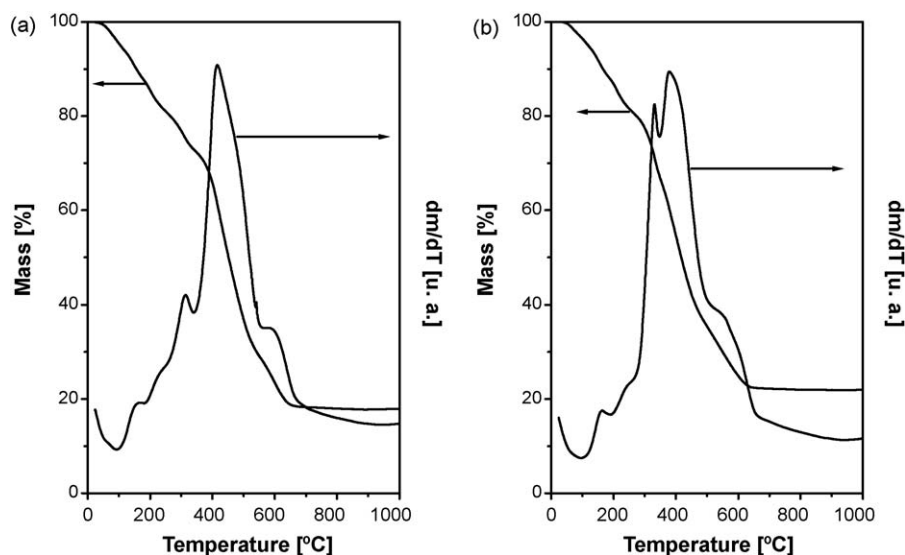


Fig. 6. TGA/DTG curves obtained under static air of the inorganic perovskite precursor/ C_{AEROSIL} composite: (a) LaFeO_3 and (b) $\text{LaFe}_{0.6}\text{Co}_{0.4}\text{O}_3$.

As reported [64–66], the transformation of perovskite precursors prepared by the citrate method occurs only in the presence of air. For that reason and to avoid the occurrence of a high rate of carbon oxidation, the calcination of the perovskite inorganic precursors/carbon C_{AEROSIL} composite was carried out under static air. As can be seen from Fig. 6, the TGA performed in such condition show the same principal mass loss steps corresponding to perovskite formation (Fig. 5), nevertheless, with a higher mass loss between 300 and 650 °C when compared with the TGA/DTG curves of the uncast perovskite precursors (Fig. 5). Taking into account the TGA/DTG results of the carbon C_{AEROSIL} (Fig. 4), the pointed mass loss increase must be attributed to the carbon oxidation. To know the extension of this carbon oxidation process, after the TGA of the inorganic precursors, the formed nanocast perovskite was cooled to room temperature and resubmitted to a new TGA under air flow. The TGA results (not shown) did not show

any mass loss, then evidencing that the carbon mould was simultaneously removed with the citrates and nitrates during the thermal treatment of the perovskite precursors.

The X-ray diffractograms of LaFeO_3 and $\text{LaFe}_{0.6}\text{Co}_{0.4}\text{O}_3$ perovskites, conventionally prepared by the citrate method or by nanocasting, are shown in Fig. 7. As can be seen, the diffractograms reveal that the crystalline perovskite structure is the main phase in all of the synthesized solids. In the diffractogram of the ternary nanocast $\text{LaFe}_{0.6}\text{Co}_{0.4}\text{O}_3$ perovskite, low intensity diffraction peaks corresponding to La_2O_3 and Fe_2O_3 are also observed. As shown in the detail of Fig. 7, the most intense diffraction peak ($2\theta \sim 32.5^\circ$) is a single peak for all of the studied perovskites, which confirms the presence of an orthorhombic structure [67]. The conventional synthesis method originates very crystalline samples showing well-resolved and high intensity XRD peaks. On the other hand, the perovskites prepared by nanocasting, in despite of their well

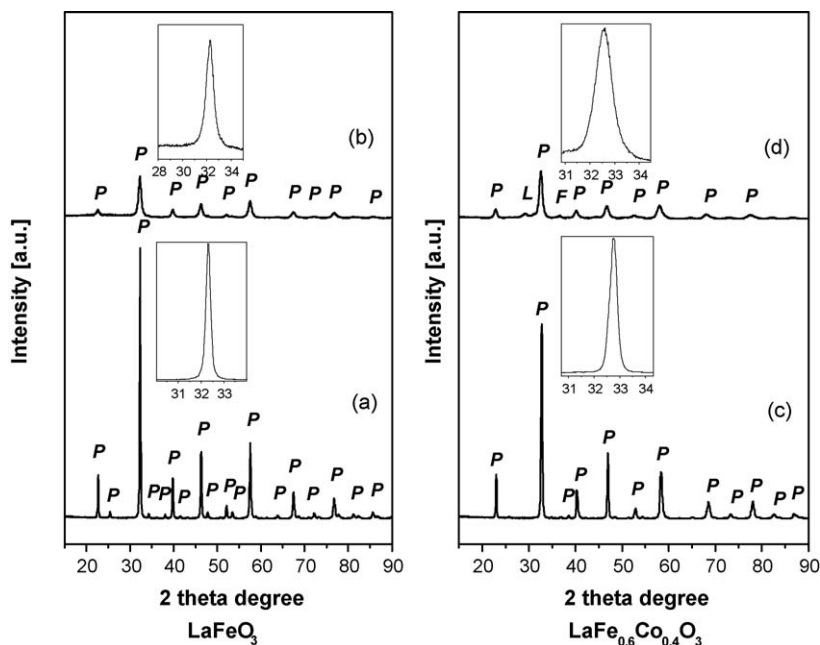


Fig. 7. XRD patterns of: (a) LaFeO_3 and (c) $\text{LaFe}_{0.6}\text{Co}_{0.4}\text{O}_3$ perovskites conventionally prepared by the citrate method; (b) LaFeO_3 and (d) $\text{LaFe}_{0.6}\text{Co}_{0.4}\text{O}_3$ nanocast perovskites. The letters refers to phases: (P) Perovskite; (L) La_2O_3 and (F) Fe_2O_3 .

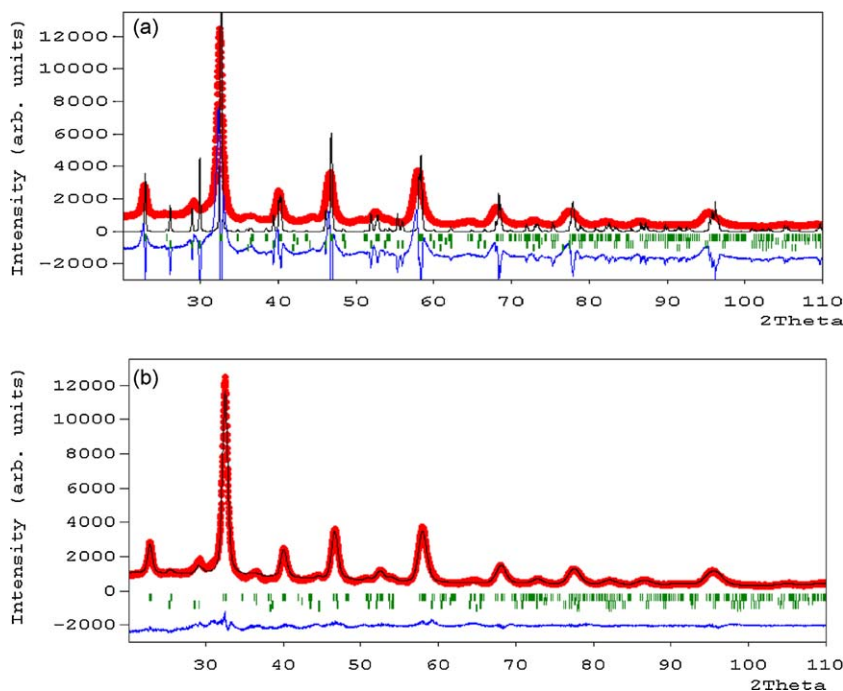


Fig. 8. Observed (dots), fitted (continuous line) and difference (bottom line) diffractograms for the nanocast $\text{LaCo}_{0.4}\text{Fe}_{0.6}\text{O}_3$ perovskite: (a) in the beginning of the refinement and (b) after the refinement was finished. The small vertical lines above the difference plots are the Bragg peak positions.

resolved XRD patterns, showed broader diffraction peaks and lower in intensity indicating that these solids are constituted by very small particles. Application of the Scherrer's formula [50] to the XRD indicates that nanocast perovskites are constituted by crystallites of about 6 nm in size.

The results of the X-ray diffraction and the Rietveld refinement performed on the nanocast $\text{LaFe}_{0.6}\text{Co}_{0.4}\text{O}_3$ perovskite are shown in Fig. 8 and Table 2. The Rietveld method [55], also known as total pattern fitting, was used here for an accurate quantitative phase analysis of the powder patterns of the mentioned nanocast perovskite, whose conventional XRD pattern above discussed showed other than the perovskite phase. Quantitative phase analysis is used to determine the concentration of various phases that are present in a mixture after the identity of every phase has been established. Scale factors for every phase present in the mixture, which are determined quite accurately during Rietveld refinement, are proportional to the fraction of the unit cells present in the irradiated volume of the sample. Thus, the scale factors can be easily converted into weight, molar or volume fractions of the

respective phase, giving the percentage of the phase in the sample [68].

The refinement was performed in the whole range of collected data. Only the scale factor, background, cell parameters and the peak profile parameters were varied; the fractional atomic coordinates and occupation factors were kept fixed. The observed and calculated diffractograms and the differences among them concerning the beginning (Fig. 8a) and the end of the refinement (Fig. 1b). The end of the refinement led to the disagreement factors (R_p , R_{wp} and R_{exp}) shown in Table 2, which also list the refined parameters (a , b , c , U , V , W). Based on the Rietveld analysis it was determined that the nanocast $\text{LaFe}_{0.6}\text{Co}_{0.4}\text{O}_3$ perovskite phase represents 97.30 wt% of the sample, while 2.70 wt% represents the presence of impurity, identified as La_2O_3 . Although were included in the Rietveld refinement phases containing the metals Co and Fe, it indicated a negligible concentration for them.

Disagreement factors (Table 2) show that the calculated and observed diffractograms are in good agreement (Fig. 8), as well as that the structure was well refined. The obtained Profile Residual

Table 2

Rietveld parameters of principal interest for the mixture of nanocast $\text{LaFe}_{0.6}\text{Co}_{0.4}\text{O}_3$ and La_2O_3 compared with the refined values of the parameters found in the literature.

Refined parameters	$\text{LaCo}_{0.4}\text{Fe}_{0.6}\text{O}_3$		La_2O_3	
	Karpinsky et al. [52]	Refinement	Hirosaki et al. [53]	Refinement
A (nm)	0.55110	0.55592	0.3936	0.4064
B (nm)	0.54660	0.54854	0.3936	0.4064
C (nm)	0.77484	0.77520	0.6166	0.6245
α (°)	90	90	90	90
β (°)	90	90	90	90
γ (°)	90	90	120	120
U^a	–	3.04934	–	0.00413
V^a	–	–0.98847	–	–0.00762
W^a	–	0.21917	–	0.00625
R_p		7.91		
R_{wp}		10.9		
R_{exp}		6.31		

^a Halfwidth parameters.

Table 3

Textural properties of the prepared perovskites.

Sample	Preparation method	Symmetry	S_{BET}^a (m ² /g)	V_p^b (cm ³ /g)
LaFeO ₃	Conventional	Orthorhombic	5.6	0.0069
LaFeO ₃	Nanocasting	Orthorhombic	49.3	0.0702
LaFe _{0.6} Co _{0.4} O ₃	Conventional	Orthorhombic	3.6	0.0045
LaFe _{0.6} Co _{0.4} O ₃	Nanocasting	Orthorhombic	30.5	0.0988

^a BET specific surface area.^b Pore volume.

(R_p) and the Weighted Profile Residual (R_{WP}) confirm good agreement between calculated and experimental diffractograms.

Since $R_p = \frac{\sum_i |y_{i(\text{obs})} - y_{i(\text{calc})}|}{\sum_i |y_{i(\text{obs})}|}$ and $R_{WP} = \left[\frac{\sum_i w_i |y_{i(\text{obs})} - y_{i(\text{calc})}|^2}{\sum_i w_i |y_{i(\text{obs})}|^2} \right]^{1/2}$, the good agreement between calculated and experimental diffractograms is due to the fact that no major discrepancies were observed between the observed and calculated intensities values y at each point i (Fig. 8). In the definition of R_{WP} , weights w_i are taking from the experimental error margins [69].

Table 3 provides the textural properties of the synthesized materials. It is observed that the nanocasting route resulted in the formation of perovskites with specific surface areas substantially higher than those samples conventionally prepared by the citrate method. As can be seen in Fig. 9, the isotherms were of type II or III (predominantly) that are typical for non-porous or macroporous solids. According to the literature [14,70], the specific surface area of perovskites correspond mainly to the external surface of the particles, which is characteristic for non-porous grains. As expected, the samples conventionally prepared by the citrate method have no internal porosity as confirmed by the lack of any isotherm hysteresis loop (Fig. 9a and c) and by the very low values of pore volume given in Table 3. Thus, for the uncast perovskites

the calculated specific surface area is due to the external porosity generated by the agglomeration of the small particles. The perovskites prepared by nanocasting show similar sorption isotherms although they have some hysteresis degree (Fig. 9b and d) and higher specific surface area and pore volume (Table 3). These improved textural properties are attributed to the templating effect of the nanocast carbon during the perovskite synthesis. In this way, the porosity measurements reveal that the use of CAEROSIL as hard template produces mainly solids with no significantly intraparticle pores but made up of very small particles. Therefore, the nanocast perovskites cannot be seen as an inverse replica of the porous carbon used as template, which contains framework-confined pores (Fig. 2 and Table 1), but as an agglomerated material formed majority by non-porous nanoparticles.

Fig. 9 also shows the pore size distribution (PSD) of the studied perovskites (as insets). As can be seen the uncast and nanocast perovskites show a broad and irregular PSD. In our experiments, the production of perovskites following the nanocasting pathway did not achieve specific surface areas higher than 50 m²/g. We attribute this result to the calcination conditions to generate the perovskite phase, which required the use of high temperatures (up

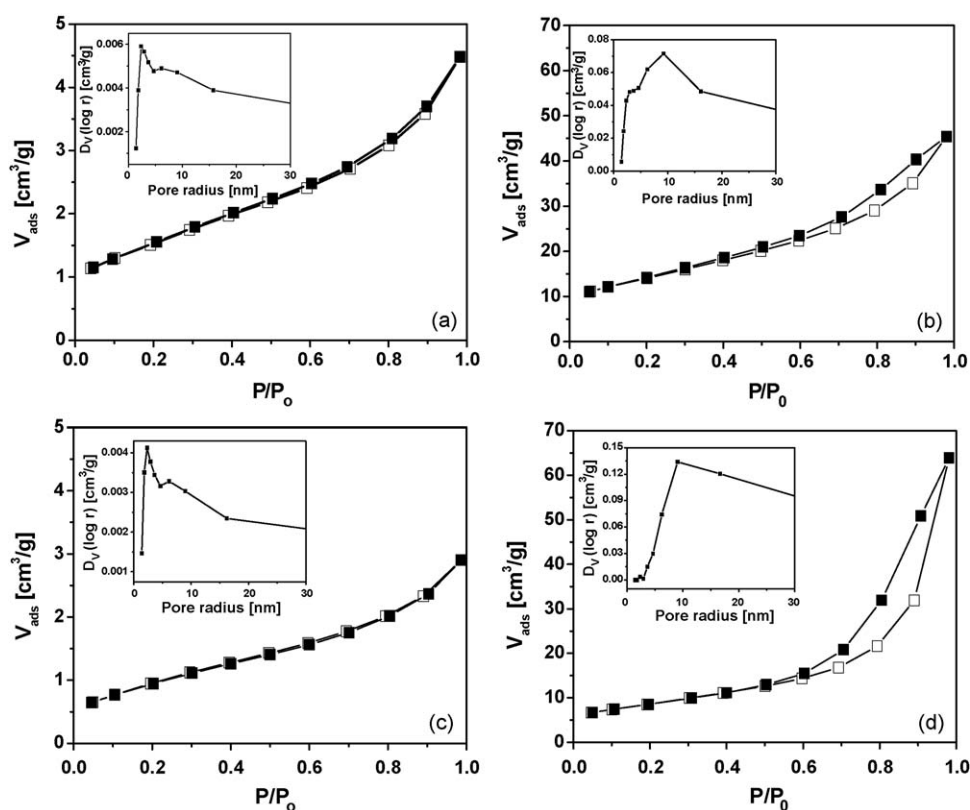


Fig. 9. Nitrogen adsorption/desorption isotherms and BJH pore size distribution of: (a) LaFeO₃ and (c) LaFe_{0.6}Co_{0.4}O₃ perovskites conventionally prepared by the citrate method; (b) LaFeO₃ and (d) LaFe_{0.6}Co_{0.4}O₃ nanocast perovskites. The symbols refer to: (■) adsorption; (□) desorption.

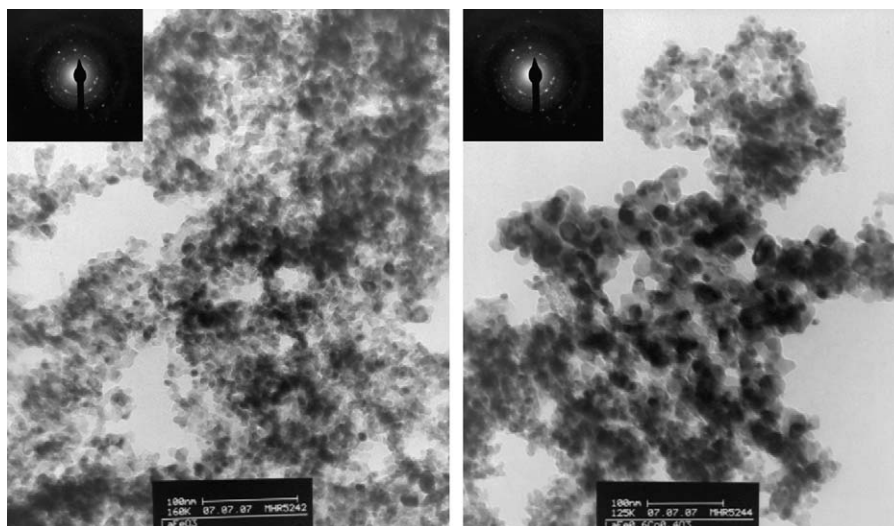


Fig. 10. TEM images of LaFeO_3 (left) and $\text{LaFe}_{0.6}\text{Co}_{0.4}\text{O}_3$ (right) nanocast perovskites. In the detail are the selected-area electron diffraction (SAED) patterns.

to 800 °C) and air atmosphere. As verified, in such conditions the transformation of the inorganic precursors to oxides occurred simultaneously with the removal of the carbon by oxidation (Fig. 6) that could facilitate subsequently the sintering of the formed perovskite nanoparticles. Thus, the confinement effect during the perovskite synthesis by nanocasting cannot be completely preserved, limiting their effect in the increase of the specific surface area. Therefore, the resulting nanocast perovskites synthesized from the procedure applied here still have relatively low surface area when compared to other nanocast oxides obtained at lower temperatures.

Transmission electron microscopy (TEM) confirms the nano-sized characteristics of the nanocast perovskites. Fig. 10 shows some representative TEM images taken from LaFeO_3 and $\text{LaFe}_{0.6}\text{Co}_{0.4}\text{O}_3$ prepared using CAEROSIL as mould. It is clear that the nanocast perovskites consist of agglomerates smaller than 100 nm, which is coherent with the results of N_2 sorption measurements. The selected-area electron diffraction (SAED) patterns consist of single spots superimposed on diffuse rings (insets in Fig. 10), indicating that the crystalline domains making part of the agglomerates are quite small, which is in agreement with the XRD data.

3.3. Perovskites activity

The catalytic behavior in the reduction of NO with CO of LaFeO_3 and $\text{LaFe}_{0.6}\text{Co}_{0.4}\text{O}_3$ perovskites conventionally or nanocasting prepared is shown in Fig. 11. As expected [22], the conversion

of NO and CO on all the studied perovskites increases with the increase of the temperature. This activity increase must be attributed only to the catalytic effect due to the fact that practically no activity is observed when the NO reduction is carried out between 200 and 700 °C without any catalyst (see inset in Fig. 11a).

From Fig. 11a it can clearly be seen that the nanocast LaFeO_3 perovskite is much more active for the reduction of NO to N_2 and for the oxidation of CO to CO_2 than the uncast LaFeO_3 one. The more remarkable is that the nanocast LaFeO_3 perovskite reaches conversions of NO or CO of about 80% at 350 °C and 100% at 400 °C. The uncast LaFeO_3 perovskite reaches 100% of conversion of NO or CO at temperatures higher than 580 °C. Considering that the catalyst tests were carried out using the same contact time and that nanocast and uncast LaFeO_3 perovskites have the same composition, the observed higher activity of the former must be related with a higher number of accessible active sites and therefore with its higher specific surface area.

Nevertheless, a strong effect of the increase of the specific surface area in the activity could not always be clearly evidenced. As can be seen from Fig. 11b, the nanocast $\text{LaFe}_{0.6}\text{Co}_{0.4}\text{O}_3$ perovskite shows only a slightly higher activity for NO and CO conversion than the uncast one. Such little increase in the activity can be attributed to the enhanced specific surface area of the nanocast $\text{LaFe}_{0.6}\text{Co}_{0.4}\text{O}_3$, which was lower 40% than that of the nanocast LaFeO_3 . On the other hand, it must be taken into consideration the presence of Co in the ternary discussed perovskites. As described by Lima [71] substitution of Fe atoms over 30% by Co atoms in the structure of La–Fe perovskites led to a

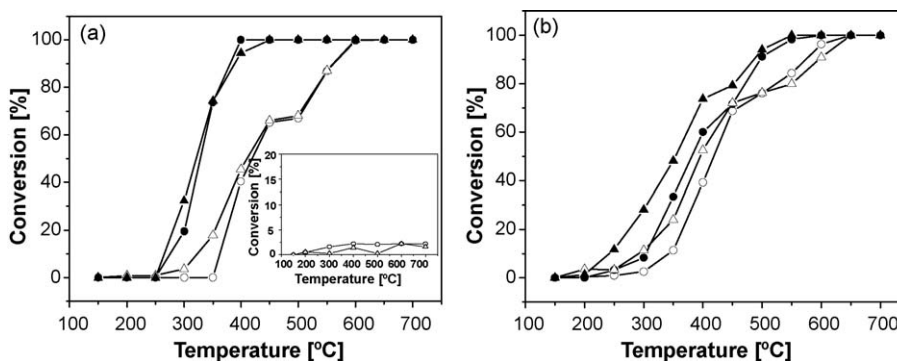


Fig. 11. Temperature profiles for the conversion of NO to N_2 (○, ●) and CO to CO_2 (△, ▲) on: (a) uncast LaFeO_3 (○, △) and nanocast LaFeO_3 (●, ▲). Inset: conversion of NO to N_2 (○) and CO to CO_2 (△) without any catalyst; (b) uncast $\text{LaFe}_{0.6}\text{Co}_{0.4}\text{O}_3$ (○, △) and nanocast $\text{LaFe}_{0.6}\text{Co}_{0.4}\text{O}_3$ (●, ▲).

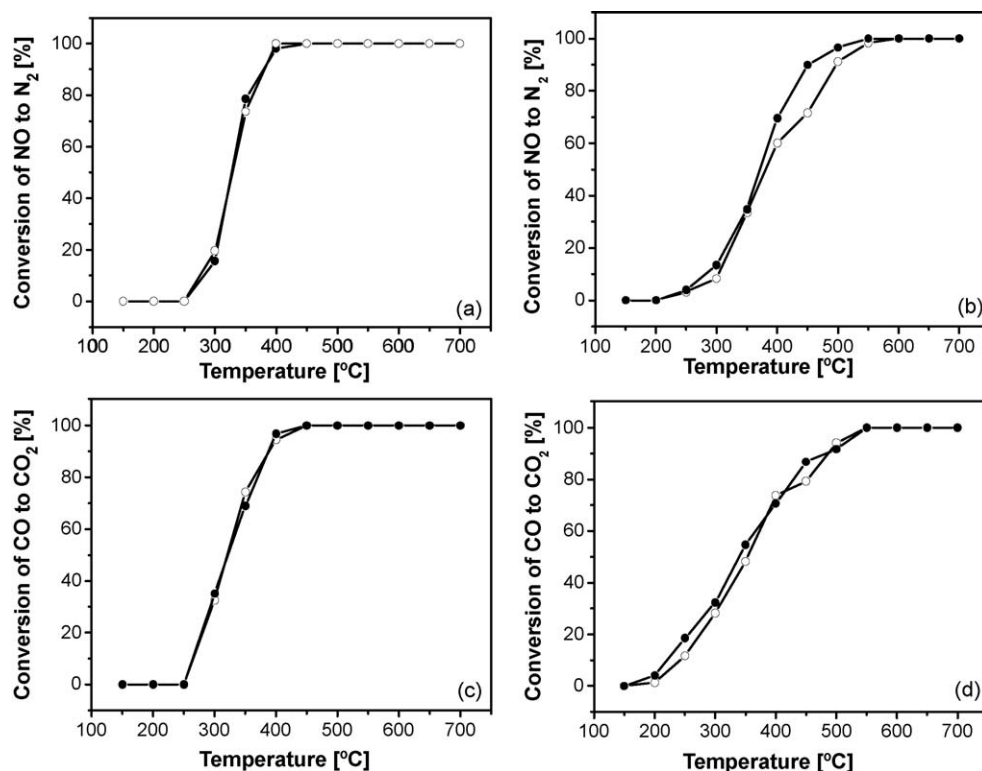


Fig. 12. Two consecutive temperature profiles for the conversion of NO to N₂ (a and b) and CO to CO₂ (c and d) on the nanocast perovskites: LaFeO₃ (a and c) and LaFe_{0.6}Co_{0.4}O₃ (b and d). Symbols (●) and (○) refers to the first and the second test, respectively.

lower activities in the studied reactions when compared with the binary La–Fe or La–Co perovskites.

Nevertheless, as verified by the XRD data (Fig. 7) and the results of the Rietveld refinement (Fig. 8 and Table 2), the nanocast LaFe_{0.6}Co_{0.4}O₃ perovskite presented as contaminant the non-active La₂O₃ outside of their structure, which in despite of their low content (2.7 wt%) could partially be blocking the perovskite active sites, then diminishing their catalytic activity.

Fig. 12 shows the results of two consecutive catalytic test done with the nanocast LaFeO₃ and LaFe_{0.6}Co_{0.4}O₃ perovskites. The reproducibility of the conversion data in the whole 150–700 °C temperature range evidences that there was no perovskite deactivation. This catalytic stability indicates that no sintering

or other physical or chemical changes occur during the NO reduction process. This behavior can be understood taking into consideration the TGA results of the inorganic perovskite precursor/carbon C_{AEROSIL}, which showed that up to 650 °C the inorganic precursor transformation simultaneously occur with the carbon oxidation (Fig. 6). Thus, as already commented, the perovskite sintering must also be taking place during the thermal treatment under static air involving heating up to 800 °C with a stay of 5 h at this temperature.

To corroborate the catalytic stability of the studied nanocast perovskites, experiments were performed during 1400 min on stream at 380 °C. At that temperature the conversion levels were lower than 100%, allowing to observe if real differences occur in the performance of the considered perovskites. As can be clearly seen in Fig. 13, the nanocast perovskites maintained unchangeable their catalytic activity in the reactions involved in the reduction of NO with CO.

4. Conclusions

The present study demonstrates that the specific surface area of perovskites can be substantially improved using in their synthesis a carbon cast in Silica Aerosil 200 as hard template. After the silica removal from the prepared silica/carbon composite, N₂ sorption measurements evidenced that the nanocast carbon is formed by mesopores with diameter in the range of 2–8 nm. A significant amount of micropores was also verified. Other hand, the nanocast perovskites did not show significantly intraparticle porosity in despite of their enhanced specific surface area with values between 30 and 50 m²/g. Nevertheless, TEM images, XRD and Rietveld refinement data showed that those solids are constituted at least by 97 wt% of perovskite phase and by agglomerates smaller than 100 nm, which are composed by nanocrystallites with diameters of about 6 nm. The synthesis of perovskites following

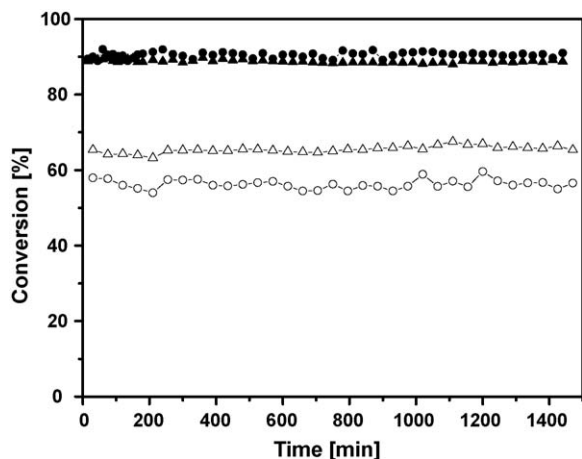


Fig. 13. Conversion at 380 °C as a function of the time on stream after two consecutive catalytic tests: NO to N₂ (○, ●) and CO to CO₂ (△, ▲) on the nanocast perovskites: LaFeO₃ (●, ▲) and LaFe_{0.6}Co_{0.4}O₃ (○, △).

the nanocasting pathway did not allow the preparation of solids with specific surface areas higher than 50 m²/g that was attributed to the calcination conditions to generate the perovskite phase, which required the use of high temperatures (up to 800 °C) and air atmosphere. In such conditions the transformation of the inorganic precursors to oxides simultaneously occurred with the removal of the carbon by oxidation that facilitates the subsequently sintering of the formed perovskite nanoparticles, thus, diminishing the template effect and limiting the increase of the specific surface area. The nanocast LaFeO₃ perovskite prepared by nanocasting was substantially more active in the reduction of NO to N₂ with CO and in the oxidation of the last compound to CO₂ than that with the same composition conventionally prepared by the citrate method. The improvement in the catalytic behavior of the nanocast LaFeO₃ was attributed to the increase in their specific surface area, which allows the exposure of a higher number of accessible active sites. However, the effect of the increase of the perovskite specific surface area in the catalytic activity must also be related with the perovskite composition and the presence of impurities, which were pointed as the responsible that impeded a more significantly increase in the activity of the nanocast LaFe_{0.6}Co_{0.4}O₃, in despite of its improved textural properties. The nanocast perovskites also showed high thermal and catalytic stability during long time on stream, corroborating their high potential as catalysts for the studied reaction.

Acknowledgments

The authors gratefully acknowledge the financial support provided by CNPq/Brazil (grant 505157/2004-7). R.K.C. Lima also gives acknowledgements to Capes/Brazil for the fellowship granted.

References

- [1] J.M.D. Tascón, J.L.G. Fierro, L.G. Tejuca, Z. Phys. Chem. N. F. 124 (1981) 249.
- [2] K. Tabata, M. Misono, Catal. Today 8 (1990) 249.
- [3] N. Misuno, M. Tanaka, M. Misono, J. Chem. Soc. Faraday Trans. 88 (1992) 91.
- [4] H. Yasuda, Y. Fujiwara, N. Mizuno, M. Misono, J. Chem. Soc. Faraday Trans. 90 (1994) 1183.
- [5] L. Forni, C. Oliva, T. Barzetta, E. Selli, A.M. Ezeretsband, A.V. Vishniakov, Appl. Catal. B: Environ. 13 (1997) 35.
- [6] L.G. Tejuca, J.L.G. Fierro (Eds.), Properties and Applications of Perovskite-type Oxides, Marcel Dekker, New York, 1993.
- [7] L. Simonot, F. Garin, G. Maire, Appl. Catal. B: Environ. 11 (1997) 181.
- [8] H. Tanaka, M. Misono, Curr. Opin. Solid State Mater. Sci. 5 (2001) 381.
- [9] M.J. Koponen, M. Suvanto, T.A. Pakkanen, K. Kallinen, T.-J.J. Kinnunen, M. Härkönen, Solid State Sci. 7 (2005) 7.
- [10] U. Russo, L. Nodaria, M. Faticanti, V. Kuncser, G. Filoti, Solid State Ionics 176 (2005) 97.
- [11] J.H. Kuo, H.U. Anderson, M. Sparlin, J. Solid State Chem. 83 (1989) 52.
- [12] J.A. Alonso, M.J. Martinez-Lopez, M.T. Casais, A. Munoz, Solid State Commun. 102 (1997) 7.
- [13] H. Dai, H. He, P. Li, L. Gao, C.-T. Au, Catal. Today 90 (2004) 231.
- [14] M.R. Goldwasser, M.E. Rivas, M.L. Lugo, E. Pietri, J. Pérez-Zurita, M.L. Cubeiro, A. Griboval-Constant, G. Leclercq, Catal. Today 107–108 (2005) 106.
- [15] C. Bernard, G. Dauzet, F. Mathieu, B. Durand, E. Puech-Costes, Mater. Lett. 59 (2005) 2615.
- [16] T. Hayakawa, S. Suzuki, J. Nakamura, T. Uchijima, S. Hamakawa, K. Suzuki, T. Shihido, K. Takehira, Appl. Catal. A 183 (1999) 273.
- [17] T. Utaka, S. Al-Drees, J. Ueda, Y. Iwasa, T. Takeguchi, R. Kikuchi, K. Eguchi, Appl. Catal. A 247 (2003) 125.
- [18] M.R. Goldwasser, M.E. Rivas, E. Pietri, J. Pérez-Zurita, M.L. Cubeiro, A. Griboval-Constant, G. Leclercq, J. Mol. Catal. A 228 (2005) 325.
- [19] B. Viswanathan, Catal. Rev. Sci. Eng. 34 (1992) 337.
- [20] M.A. Pena, J.L.G. Fierro, Chem. Rev. 101 (2001) 1981.
- [21] N.K. Labhsetwar, A. Watanabe, R.B. Biniwale, R. Kumar, T. Mitsuhashi, Appl. Catal. B 33 (2001) 165.
- [22] V.I. Părvulescu, P. Grange, B. Delmon, Catal. Today 46 (1998) 233.
- [23] W.P.A. Jansen, J.M.A. Harmsen, A.W.D.V.D. Gon, J.H.B.J. Hoebink, J.C. Schouten, H.H. Brongersma, J. Catal. 204 (2001) 420.
- [24] H.S. Gandhi, G.W. Graham, R.W. McCabe, J. Catal. 216 (2003) 433.
- [25] R. Zhang, A. Villanueva, H. Alamdari, S. Kaliaguine, J. Mol. Catal. A 258 (2006) 22.
- [26] Y. Teraoka, H. Nii, S. Kagawa, K. Jansson, M. Nygran, Appl. Catal. A 194 (2000) 35.
- [27] A.E. Giannakas, A.K. Ladavos, P.J. Pomonis, Appl. Catal. B 49 (2004) 147.
- [28] A.E. Giannakas, A.A. Leontiou, A.K. Ladavos, P.J. Pomonis, Appl. Catal. A 309 (2006) 254.
- [29] M. Schwickardi, T. Johann, W. Schmidt, F. Schüth, Chem. Mater. 14 (2002) 3913.
- [30] A.E. Giannakas, T.C. Vaimakis, A.K. Ladavos, P.N. Trikalitis, P.J. Pomonis, J. Colloid Interface Sci. 259 (2003) 244.
- [31] X. Li, H.B. Zhang, X.X. Liu, S.J. Li, M.Y. Zhao, Mater. Chem. Phys. 38 (1994) 355.
- [32] C. Xiulan, L. Yuan, Chem. Eng. J. 78 (2001) 205.
- [33] G. Sinquin, C. Petit, J.P. Hindermann, A. Kienemann, Catal. Today 70 (2001) 183.
- [34] J. Kirchenova, D. Kwana, J. Vaillancourt, J. Chaouki, Catal. Lett. 21 (1993) 77.
- [35] J. Kirchenova, D. Kwana, Int. J. Hydrogen Energy 19 (1994) 501.
- [36] R. Leanza, I. Rossetti, L. Fabrin, C. Oliva, L. Forni, Appl. Catal. B 28 (2000) 55.
- [37] J. Roggenbuck, H. Schäfer, T. Tsoncheva, C. Minchev, J. Hanss, M. Tiemann, Micropor. Mesopor. Mater. 101 (2007) 335.
- [38] B. Tian, X. Liu, H. Yang, S. Xie, C. Yu, B. Tu, D. Zhao, Adv. Mater. 15 (2003) 1370.
- [39] J.-H. Smätt, C. Weidenthaler, J.B. Rosenholm, M. Lindén, Chem. Mater. 18 (2006) 1443.
- [40] C. Dickinson, W. Zhou, R.P. Hodgkins, Y. Shi, D. Zhao, H. He, Chem. Mater. 18 (2006) 3088.
- [41] T. Valdés-Solís, A.B. Fuertes, Mater. Res. Bull. 41 (2006) 2187.
- [42] Y. Xia, R. Mokaya, J. Mater. Chem. 15 (2005) 3126.
- [43] B.K. Cho, B.H. Shanks, J.E. Bailey, J. Catal. 115 (1989) 489.
- [44] B.K. Cho, J. Catal. 131 (1991) 74.
- [45] E. Novak, D. Sprinceana, F. Solymosi, Appl. Catal. A 149 (1997) 89.
- [46] K. Takehira, T. Hayakawa, H. Harihara, A.G. Andersen, K. Suzuki, M. Shimizu, Catal. Today 24 (1995) 237.
- [47] J.-S. Yu, S.B. Yoon, G.S. Chai, Carbon 39 (2001) 144.
- [48] Anonymous, Aerosil–Pyrogene Kieselsäuren, Degussa AG, Hanau, unknown year.
- [49] JCPDS—Joint Committee on Powder Diffraction Standards, International Center of Diffraction Data, Pennsylvania, USA, 1994.
- [50] B.D. Cullity, Elements of X-ray Diffraction, Addison-Wesley Pub. Comp. Inc., EUA, 1967.
- [51] H.M.J. Rietveld, Appl. Cryst. 14 (1981) 357.
- [52] D.V. Karpinsky, I.O. Troyanchuk, M. Kopcewicz, Phys. Status Solidi B 244 (4) (2007) 1409.
- [53] N. Hirosaki, S. Ogata, C.J. Kocer, Alloy Compd. 351 (1–2) (2003) 31.
- [54] Rodríguez-Carvajal, J. FullProf Program: Rietveld, Profile Matching and Integrated Intensities Refinement of X-Ray and/or Neutron Data (powder and/or single-crystal). Laboratoire Leon Brillouin (CEA-CNRS), version September 2007.
- [55] L.B. McCusker, R.B. Von Dreele, D.E. Cox, D. Louerd, P.J. Scardie, Appl. Cryst. 32 (1999) 36.
- [56] G.S. Pawley, J. Appl. Cryst. 14 (1981) 357.
- [57] ICSD 2008. Available at <http://www.fiz-karlsruhe.de/icsd.html> or <http://icsd-web.fiz-karlsruhe.de>
- [58] P. Thompson, D. Cox, J.J. Hastings, Appl. Cryst. 20 (1987) 79.
- [59] S. Brunauer, P.H. Emmet, E. Teller, J. Am. Chem. Soc. 60 (1938) 1553.
- [60] E.P. Barret, L.G. Joyner, P.P. Halenda, J. Am. Chem. Soc. 73 (1951) 373.
- [61] M. Hesse, H. Meier, B. Zeeh, Spektroskopische Methoden in der Organischen Chemie, Thieme, Stuttgart, 1979.
- [62] A. Johnson, E.S. Brigham, P.J. Ollivier, T.E. Mallouk, Chem. Mater. 9 (1997) 2448.
- [63] W.C. Li, A.H. Lu, S.C. Guo, Carbon 39 (2001) 1989.
- [64] R. Hammami, S.B. Aïssa, H. Batis, Appl. Catal. A 353 (2009) 145.
- [65] Y. Li, L. Xue, L. Fan, Y. Yan, J. Alloys Compd. (2008), doi:10.1016/j.jallcom.2008.11.068.
- [66] H.-F. Yu, J. Wang, S.-S. Wang, Y.-M. Kuo, J. Phys. Chem. Solids 70 (2009) 218.
- [67] N.A. Merino, B.P. Barbero, P. Ruiz, L.E. Cadús, J. Catal. 240 (2006) 245.
- [68] J.I. Langford, D. Louer, Rep. Prog. Phys. 59 (1996) 131.
- [69] E. Jansen, W. Schafer, D.G. Will, J. Appl. Cryst. 27 (1994) 492.
- [70] L. Bedel, A.C. Roger, C. Estournes, A. Kienemann, Catal. Today 85 (2003) 207.
- [71] R.K.C. Lima, Thesis, Federal University of Sao Carlos, Brazil, 2008.